Applied Surface Science 368 (2016) 36–43

Contents lists available at ScienceDirect

Applied Surface Science

journal homepage: www.elsevier.com/locate/apsusc

Biomolecule nanoparticle-induced nanocomposites with resistive switching nonvolatile memory properties

Yongmin Ko[a], Sook Won Ryu[b,*], Jinhan Cho[a,*]

[a] Department of Chemical & Biological Engineering, Korea University, Anam-dong, Seongbuk-gu, Seoul 136-713, Republic of Korea
[b] Department of Laboratory Medicine, Kangwon National University School of Medicine, Kangwondaehak-gil, Chuncheon-si, Gangwon-do 200-701, Republic of Korea

ARTICLE INFO

Article history:
Received 17 December 2015
Accepted 26 January 2016
Available online 28 January 2016

Keywords:
Nonvolatile memory
Thermal calcination
Fe_2O_3 nanocomposite
Electrostatic layer-by-layer assembly
Multilayers

ABSTRACT

Resistive switching behavior-based memory devices are considered promising candidates for next-generation data storage because of their simple structure configuration, low power consumption, and rapid operating speed. Here, the resistive switching nonvolatile memory properties of Fe_2O_3 nanocomposite (NC) films prepared from the thermal calcination of layer-by-layer (LbL) assembled ferritin multilayers were successfully investigated. For this study, negatively charged ferritin nanoparticles were alternately deposited onto the Pt-coated Si substrate with positively charged poly(allylamine hydrochloride) (PAH) by solution-based electrostatic LbL assembly, and the formed multilayers were thermally calcinated to obtain a homogeneous transition metal oxide NC film through the elimination of organic components, including the protein shell of ferritin. The formed memory device exhibits a stable ON/OFF current ratio of approximately 10^3, with nanosecond switching times under an applied external bias. In addition, these reversible switching properties were kept stable during the repeated cycling tests of above 200 cycles and a test period of approximately 10^5 s under atmosphere. These solution-based approaches can provide a basis for large-area inorganic nanoparticle-based electric devices through the design of bio-nanomaterials at the molecular level.

1. Introduction

Ferritin is a ubiquitous, intracellular iron storage protein consisting of 24-mer globular protein of H (heart or heavy) and L (liver or light) protein subunits that assemble to form a protein shell with a hollow interior of approximately 8 nm, wherein iron ions form crystallites together with phosphate and hydroxide. This ferritin can accommodate up to 4500 iron (Fe^{3+}) ions in principle; in addition, Fe ions within ferritin can be easily replaced by various types of nanosized transition metal ions using ion exchange [1–6]. As a result, ferritin has been widely employed as a template for the synthesis of nanoparticles (NPs), such as magnetic, conducting, and semiconducting nanoparticles, which can be applied in areas ranging from biomedical chemistry to integration of the structure into electronic devices [7–10]. Recently, using these unique properties of ferritin, there have been a few efforts to use ferritin-induced nanoparticles for preparation of the nonvolatile memory cells that have been widely used in a variety of mobile electronics. For example, it was reported that the iron oxide or cobalt oxide nanoparticles formed from calcinated ferritins could be used as charge storage nodes for floating-gate-type nonvolatile memory devices [11,12] composed of the following: silicon substrates, tunneling oxides, dielectric layers, charge storage nodes, blocking oxides, and gate electrodes. However, studies on nanoparticle-based memory devices with the flash memory type have mainly focused on single-layered charge trap elements. These devices typically provide a relatively low number density due to the confined lateral dimension of the single layer and resultantly have difficulty in enhancing memory performance.

Recently, resistive switching nonvolatile memory (RSNM) devices have been recognized as notable candidates for the next-generation nonvolatile memory devices because of their simple device structure, low operating voltages (<5 V), high ON/OFF current ratio (>10^2), and fast nanosecond switching times [13–19]. Notably, the operation system and physics of RSNM devices are quite different from those of the floating-gate-type nonvolatile memory devices, with a relatively high operating voltage of greater than 10 V and microsecond switching times. Although traditional RSNM devices based on transition metal oxides (TMOs), such as

* Corresponding authors.
E-mail addresses: ryusw@kangwon.ac.kr (S.W. Ryu), jinhan71@korea.ac.kr (J. Cho).

http://dx.doi.org/10.1016/j.apsusc.2016.01.225
0169-4332/

TiO_x [20,21], ZrO_x [22,23], and NiO [24,25], have primarily been prepared using the traditional methods of conventional sputtering or metal organic chemical vapor deposition, such approaches have much difficulty in producing large-area devices with a simplified manufacturing process and low cost, in spite of their excellent thermal stability and operating durability in air environments. In addition, even though it has been reported that the memory layer of RSNM devices could also be prepared by TMO NPs synthesized in organic solvent [26,27], their memory performance (ON/OFF current ratio < 10^1) was inferior to that of the vacuum-deposited devices.

Herein, we report the first success in RSNM devices using ferritin NP nanocomposites (NCs) with multi-structure. Although traditional RSNM devices based on transition metal oxide films have been mainly prepared using the conventional methods as mentioned above, our approach is based on calcinated ferritin NCs manufactured using the layer-by-layer (LbL) assembly method. Using the LbL assembly method as a solution-dipping process has been demonstrated to be quite useful for preparing organic and/or inorganic NC films with tailored electrical properties and layer thicknesses in addition to various functional components on substrates of different sizes and shapes [28–31]. For this study, positively charged poly(allylamine hydrochloride) (PAH, M_w = 56,000; Aldrich) was alternately LbL-assembled with negatively charged ferritin on a platinum (Pt) electrode to prepare the iron oxide NC (Fe_2O_3 NC) devices via calcinations of PAH/ferritin multilayers. A top electrode was deposited onto $(Fe_2O_3$ NC$)_n$ multilayer films to complete the device fabrication. These devices exhibited a memory performance with a high ON/OFF current ratio of greater than 10^2, a rapid switching speed (nanoseconds), low operating voltages of less than 2 V, and good memory stability. In this case, ferritin-induced NC devices contained no additional components, such as dopants and metal or metal oxide NPs. Furthermore, considering that the memory performance of ferritin-induced devices can be easily adjusted by changing the bilayer number, we believe that our approach can provide a basis for the fabrication of large-area RSNM devices that allow for memory modulation with a facile process and enables the development of a new field of study related to ferritin-derived nanomaterials.

2. Experimental details

2.1. Build-up of PAH/ferritin multilayers

The solution pH and concentration of PAH ($M_w \approx 56{,}000$; Aldrich) and ferritin (from equine spleen; Aldrich) were adjusted to 9 and 1 mg mL^{-1}, respectively. In this case, PAH was used as the cationic component, and ferritin was used as the anionic component. All substrates were initially cleaned using an ultraviolet (UV)-ozone cleaner. For layer-by-layer assembly, a cleaned (negatively charged) substrate was first immerged in a PAH solution for 10 min. The PAH-coated substrate was washed in deionized (DI) water to remove the loosely adsorbed molecules. Sequentially, the PAH-coated substrate was dipped in ferritin solution for 10 min and then washed with DI water, resulting in the $(PAH/ferritin)_1$ films. These cycles were repeated until multilayers with the desired bilayer number (n) were obtained.

2.2. Quartz crystal microgravimetry (QCM)

The quantitative growth of the multilayers was monitored via quartz crystal microgravimetry (QCM200, SRS). The mass changes (Δm) of each layer adsorbed onto the QCM electrode (resonance frequency is approximately 5 MHz) were obtained from the frequency change (ΔF) using the Sauerbrey equation:

$$\Delta F\,(\mathrm{Hz}) = -\frac{2F_0^2}{A\sqrt{\rho_q \mu_q}} \cdot \Delta m$$

where F_0 is the resonant frequency of the fundamental mode (in Hz). A, ρ_q, and μ_q represent the electrode area, density of quartz (2.648 g cm^{-3}), and shear modulus of quartz (2.947×10^{11} g cm^{-1} s^{-1}), respectively. These constant components indicate the sensitivity factor for the crystal and can be calculated by 56.6 Hz μg^{-1} cm^2 for a 5-MHz QCM quartz crystal at room temperature. Therefore, this equation can be simplified as follows:

$$\Delta F\,(\mathrm{Hz}) = -56.6 \Delta m_A$$

where Δm_A is the mass change per quartz crystal unit area in μg cm^{-2}.

2.3. Characterization

X-ray photoelectron spectroscopy (XPS) was conducted using an AXIS-Hsi (KRATOS) instrument, and the obtained data set was plotted after calibration based on the C 1s peak at 284.5 eV. The film thickness and the surface morphology were monitored using scanning electron microscopy (SEM, Hitachi S-4300). The crystalline nature and structure of the Fe_2O_3 NC films were confirmed using cross-sectional high-resolution transmission electron microscopy (HR-TEM, Tacnai F20). The samples were prepared using a focused ion beam (FIB; JEOL JIB-4601F). The composition of the PAH/ferritin multilayers was investigated via thermal gravimetric analysis (TGA; TA 50) at a heating rate of 10 °C min^{-1} under an N_2 atmosphere. The magnetism of the Fe_2O_3 NC was measured using a superconducting quantum interface device (SQUID; MPMS5) magnetometer with a magnetic field strength of −4000 to +4000 Oe. The atomic force microscope (AFM) measurement was performed using an XE-100 (Park Systems) instrument. Topographic images of the Fe_2O_3 NC films were obtained under the tapping mode. The conducting filamentary paths were monitored in contact current-sensing AFM (CS-AFM) mode with Pt tips.

2.4. Preparation of iron oxide nanocomposite RSNM devices

An iron oxide (Fe_2O_3) NC film electrode was prepared via thermal annealing of the PAH/ferritin multilayers deposited onto a Pt-coated silicon substrate (2×2 cm^2) at 450 °C for 2 h under an N_2 atmosphere. The resistive switching behavior was measured using a semiconductor parametric analyzer (Agilent 4155B) under a compliance current of 100 mA at room temperature, and an electrochemical non-active tungsten electrode (diameter of 50 μm) was used as the top electrode. The pulsed-voltage dependence of the high and low current level was monitored by a semiconductor parametric analyzer (HP 4155A) and a pulse generator (Agilent 81104A) at room temperature.

3. Results and discussion

The isoelectric point (pI) of ferritin is in the pH range of 4.5–4.8. Therefore, ferritin has an overall positive charge at pH < 4.5 and a negative charge at pH > 5. Fig. 1a shows an HR-TEM image of 12-nm-sized ferritin with a protein shell. In addition, it is well known that the pK_a (i.e., the pH value at which 50% of polymer's functional groups are ionized) of PAH in bulk solution is approximately 9. These phenomena indicate that ferritin and PAH can be used as negatively and positively charged species at a pH of 9, respectively. The deposition of successive PAH/ferritin layers

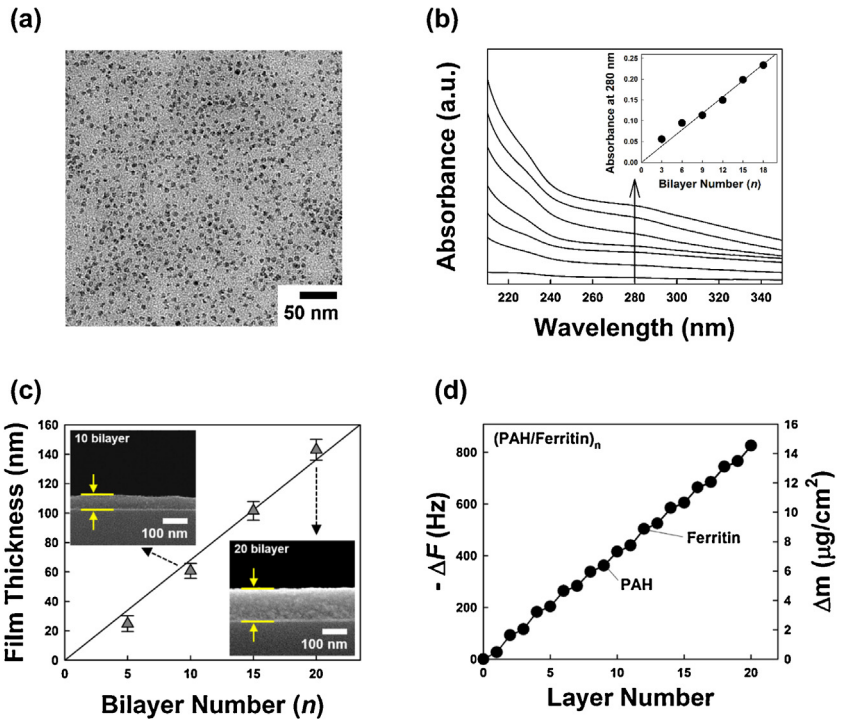

Fig. 1. (a) HR-TEM image of the approximately 12-nm ferritin nanoparticles. (b) UV–vis spectra of $(PAH/ferritin)_n$ multilayers as a function of bilayer number. The inset indicates the linear growth of the UV–vis absorbance measured at 280 nm. (c) The film thicknesses measured from cross-sectional SEM images of $(PAH/ferritin)_n$ multilayers with n increasing from 5 to 20. (d) QCM data regarding a $(PAH/ferritin)_n$ multilayer film.

based on this pH-dependent electrostatic property was characterized via UV–vis spectroscopy. The broad absorbance peak at 280 nm originates from the organic components of ferritin [32]. As shown in Fig. 1b, the uniform growth of the absorbance at 280 nm indicates that the adsorbed amount of ferritin per bilayer is regular, thus demonstrating the growth of PAH/ferritin multilayers. The absorbance measured from 280 nm grows linearly with increasing number of bilayer of PAH/ferritin (the inset of Fig. 1b). The total film thickness increased from 26 to 143 nm as the bilayer number (n) was increased from 5 to 20, as confirmed by cross-sectional SEM images of the multilayers (Fig. 1c). The quantitative growth of multilayers was monitored via the frequency changes ($-\Delta F$) in the quartz crystal microbalance (QCM) (Fig. 1d). Furthermore, the mass changes were calculated from the QCM frequency changes using the Sauerbrey equation (see Section 2). In this case, the alternating deposition of PAH and ferritin resulted in $-\Delta F$ of 21 ± 5 (Δm of $\sim$390 ng cm^{-2}) and 63 ± 4 Hz (Δm of $\sim$1064 ng cm^{-2}), respectively, per layer.

The PAH/ferritin multilayers were easily converted into iron oxide films when annealed at 450 °C for 2 h, whereas the PAH (the thermal degradation temperature of PAH is $\approx$240 °C) and protein layers of ferritin underwent thermal degradation. As confirmed from the XPS pattern of the calcinated PAH/ferritin multilayers (Fig. 2a), the spectral shape and binding energies of the significant peaks of Fe $2p_{3/2}$ (711.0 eV), Fe $2p_{1/2}$ (724.4 eV), and satellite band approximately 8 eV above the Fe $2p_{3/2}$ (719.0 eV), which is characteristic for Fe^{3+} ion in Fe_2O_3 [33–37], exhibited good agreement with previously reported data for Fe_2O_3 nanoparticles [38,39] and nanotubes [40,41]. Furthermore, the HR-TEM lattice image of the calcinated PAH/ferritin film also confirmed the formation of (1 0 4) Fe_2O_3 nanoparticles (lattice spacing: 2.70 Å) (Fig. 2b). Based on these results, the thermal decomposition of PAH/ferritin multilayers was quantitatively investigated using thermogravimetric analysis (TGA). For this investigation, electrostatically aggregated PAH-ferritin NC was first prepared at a mass ratio of the NC determined from the amount of PAH (i.e., Δm of $\sim$390 ng cm^{-2}) and ferritin (i.e., Δm of $\sim$1064 ng cm^{-2}) adsorbed in the LbL multilayers, as mentioned above. As shown in Fig. 2c, the PAH/ferritin multilayers with the isothermal treatment at 450 °C for 2 h exhibited an almost negligible decrease in the residual mass between 450 and 600 °C. In this case, the total mass of the Fe_2O_3 NC was decreased to approximately 8.47% of the initial mass of PAH/ferritin NCs. In contrast, the total film thickness of the calcinated $(PAH/ferritin)_{15}$ films was decreased to approximately 27% of the initial film thickness (Fig. 2d), thus indicating the presence of vacancy among α-Fe_2O_3 (hematite) nanoparticles with a diameter of approximately 8 nm formed after calcinations. This phenomenon was also confirmed by the tilted SEM images of the calcinated films (Fig. 2e). In this case, the root-mean-square (RMS) surface roughness of the calcinated multilayer films quantified from AFM topographic images was measured to be approximately 1.72 nm in the area of 1×1 μm^2 (Fig. 2f). The RMS surface roughness of this uniform and smooth surface of the calcinated films was slightly increased from 2.03 to 2.13 nm in an area of 5×5 μm^2 with the bilayer number was increased from 20 to 50 (Fig. S1). However, the surface roughness in the measured area did not exceed 3 nm, which indicates the homogeneity of the calcinated films.

The magnetization of the Fe_2O_3 NC film prepared from calcinated $(PAH/ferritin)_{15}$ multilayers was examined via superconducting quantum interference device magnetometry (SQUID). The magnetization curves of the multilayered films measured at room temperature (T = 300 K) were reversible without coercivity, remanence, or hysteresis, thus suggesting typical superparamagnetic behavior, as shown in Fig. 3a. At liquid helium temperature (T = 5 K), the thermally activated magnetization flipping properties of the Fe_2O_3 nanoparticles revealed frustrated superparamagnetic properties. The magnetization curves acquired a loop shape with distinct separation of the two sweeping directions, as typically

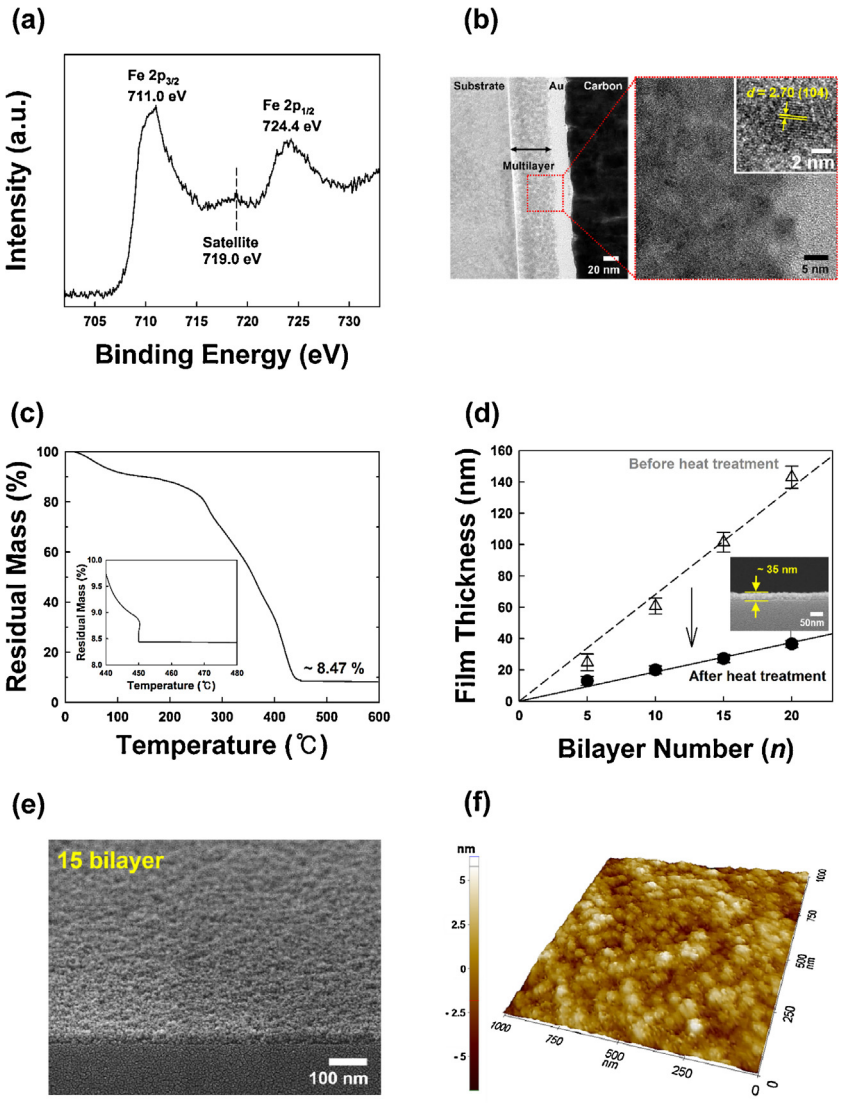

Fig. 2. (a) XPS and (b) HR-TEM lattice images of a Fe_2O_3 NC film prepared from calcinated PAH/ferritin multilayers. (c) Thermogravimetric analysis of aggregated PAH-ferritin powder with a mass ratio of approximately 1:2.7. The inset indicates the change in residual mass of aggregated powder during the isothermal process (at 450 °C for 2 h). The heating rate of TGA was 10 °C min^{-1}. (d) Film thicknesses measured from cross-sectional SEM images of calcinated $(PAH/ferritin)_n$ multilayers with n increasing from 5 to 20. (e) Tilted SEM image of calcinated $(PAH/ferritin)_{15}$ multilayers. (f) AFM topographic image of calcinated $(PAH/ferritin)_{15}$ multilayers.

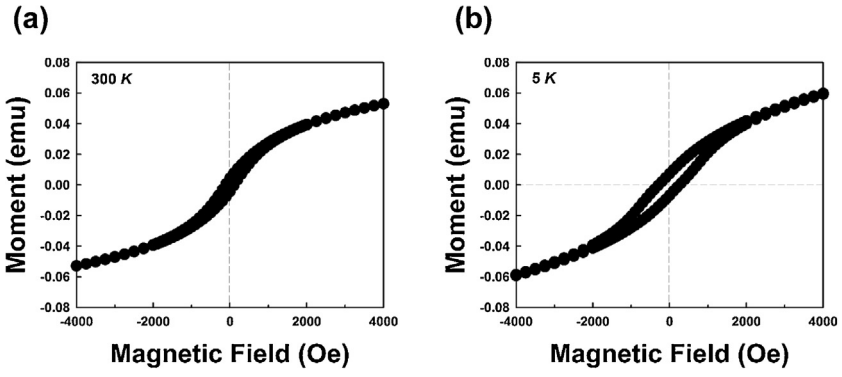

Fig. 3. The magnetization curves of calcinated PAH/ferritin multilayer films measured at (a) 300 K and (b) 5 K.

observed with ferromagnets (Fig. 3b). These results evidently imply that the calcinated films preserve the intrinsic magnetic properties (i.e., superparamagnetic properties) of isolated nanoparticles.

Based on these results, we investigated the resistive switching nonvolatile memory properties of Fe_2O_3 NC films prepared from $(PAH/ferritin)_n$ multilayers. It was reported that iron oxide nanoparticles <10 nm in size without any organic components, including surface stabilizers, were pressed into compact pellets, and the resulting nanoparticle pellets exhibited relatively high resistivity (>50 MΩ cm) due to the nanosize effect. Considering that

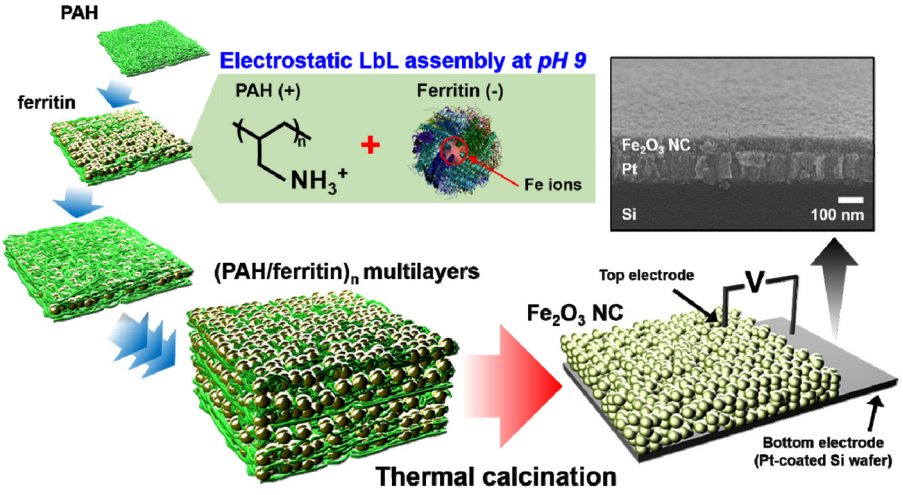

Scheme 1. Schematics for the set-up of calcinated PAH/ferritin multilayer-based nonvolatile memory devices using a tungsten-tip top electrode. The SEM image indicates the Fe_2O_3 NC film deposited onto the Pt-coated Si substrate.

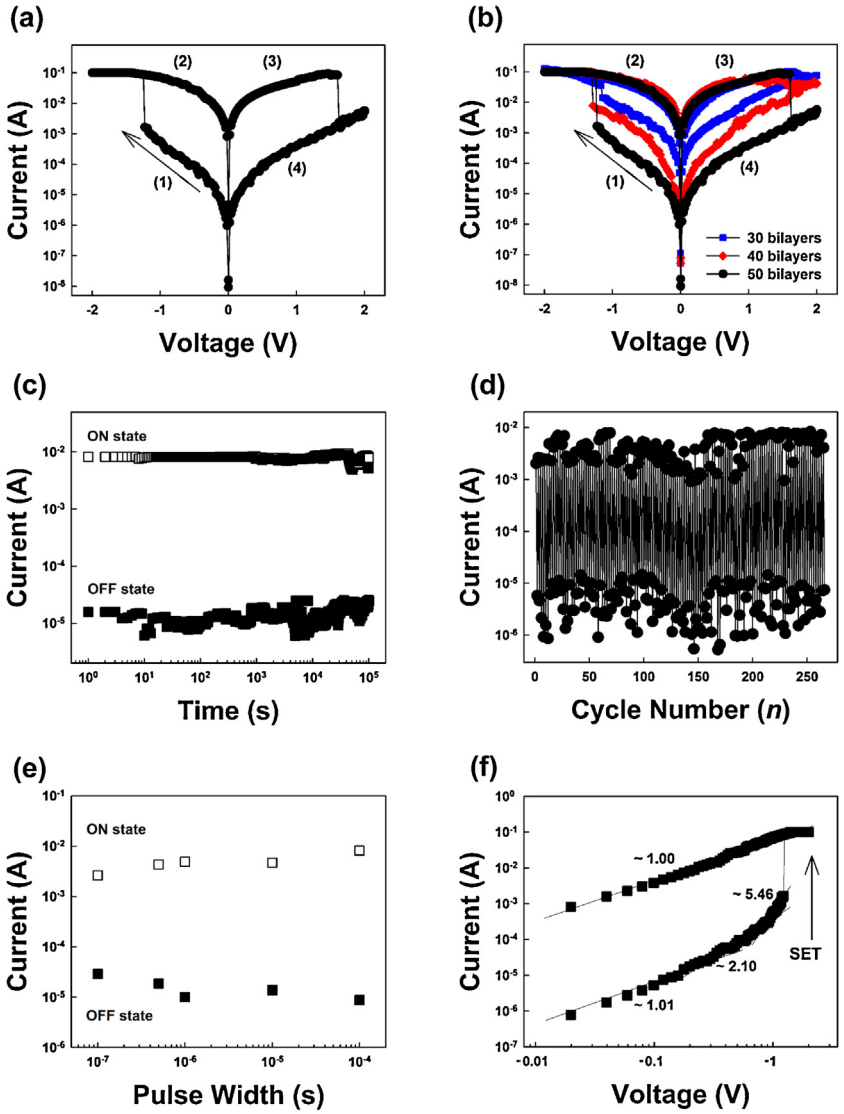

Fig. 4. (a) *I–V* curves of $(Fe_2O_3\ NC)_{50}$ film devices prepared from calcinated $(PAH/ferritin)_{50}$ multilayers. (b) *I–V* curves of $(Fe_2O_3\ NC)_n$ film devices as a function of bilayer number (n) (i.e., film thickness) for bilayer numbers of 30, 40, and 50. In this case, the low-current level (i.e., 'OFF' state) gradually decreased because the electric field strength decreased as the film thickness (i.e., bilayer number (n)) was increased. (c) Retention time and (d) cycling tests of $(Fe_2O_3\ NC)_{50}$ film devices measured at a switching speed of 100 ns at a reading voltage of +0.1 V. (e) ON/OFF current values at a reading voltage of 0.1 V for different pulse widths of 100 ns, 500 ns, 1 μs, 10 μs, and 100 μs. (f) The linear fitting for the *I–V* curve of $(Fe_2O_3\ NC)_{50}$ film devices plotted on a log–log scale for the SET process during a negative voltage sweep.

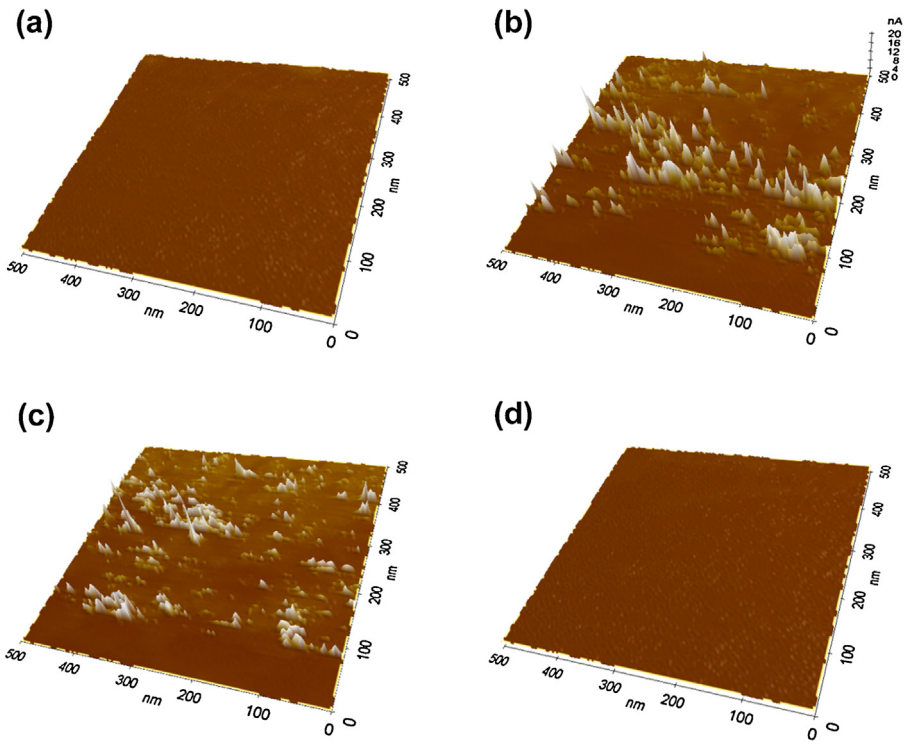

Fig. 5. CS-AFM images of Fe_2O_3 NC films with applied voltages of (a) −0.1 V (OFF state), (b) −2.0 V (ON state), (c) +1.5 V (ON state), and (d) +0.1 V (OFF state).

Fe_2O_3 films prepared from calcinations exhibited the superparamagnetic properties of ~8 nm nanoparticles, it was expected that these films would exhibit the nonvolatile memory performance exhibited by conventional resistive switching memory devices with a structure of metal bottom electrode/highly resistive transition metal oxide film/metal top electrode. For this investigation, we prepared resistive switching memory devices based on Fe_2O_3 NC films deposited onto Pt-coated substrates (Scheme 1). To complete the device fabrication, we employed an electrochemically inert tungsten tip (~10 μm) as the top electrode instead of a vacuum-deposited metal electrode. The tungsten tip electrode allows for physical contact with the film while eliminating the possibilities of metal ion diffusion into the porous Fe_2O_3 NC films and the switching behavior induced by an electrochemical redox reaction exhibited in electrochemically active Ag electrodes.

For the measurement of typical bipolar switching (i.e., switching behavior that depends on the polarity of the applied voltage), voltage sweeps from 0 to −2 V and back to +2 V were applied, with the current compliance limited to be less than 100 mA. As shown in Fig. 4a, the low-current state, i.e., the 'OFF' state (step (1)), was suddenly converted to a high-current state (SET process for 'ON' state) at −1.2 V. This ON state after the SET process was maintained from −2.0 to +2.0 V (steps (2) and (3)) when the polarity of the voltage applied to the Fe_2O_3 NC films was reversed at +2.0 V. However, the high-current state was abruptly switched to a low-current state (RESET process for 'OFF' state) at +1.6 V. The increase in the layer number largely decreased the current level, mainly the OFF current level, because the strength of the electric field across the Fe_2O_3 NC films decreased with increasing film thickness (Fig. 4b). Fig. 4c and d shows that the ON and OFF states remained stable during the entire test period of 10^5 s and the cycling test of 270 times under ambient conditions, respectively. The ratio of the current in the ON state to that in the OFF state was approximately 10^3, and these devices were operated repeatedly with switching times ranging from 100 ns to 100 μs (Fig. 4e). These reversible switching properties were maintained for longer than 1 month (Fig. S2), thus demonstrating electrical stability with a rapid switching speed.

To understand the conducting behavior of the Fe_2O_3 NC films, the nonlinear *I–V* characteristics in the negative voltage sweep region were plotted on a log–log scale. Fig. 4f shows that the *I–V* relationship in the ON state clearly exhibited Ohmic conduction behavior with a slope of 1.00, which was attributed to the formation of conducting paths in the device during the SET process. However, the conducting behavior in the OFF state was much more complicated. The fitting results for the OFF state exhibited charge transport behavior similar to that of space charge-limited conduction (SCLC), which consists of three different regions: an Ohmic region ($I \propto V$), a Child's law region ($I \propto V^2$), and a sharp current increase region (i.e., the traps-filled limit). The totally different conduction behavior in the ON and OFF states also suggests that the high conductivity in the ON-state device was a localized conducting effect rather than a homogeneously distributed one. To clearly confirm the resistive switching feature of the Fe_2O_3 NC film devices mentioned above, the formation and rupture of the local filamentary conducting channels within the Fe_2O_3 NC film were optically monitored via CS-AFM over a $0.5 \times 0.5\ \mu m^2$ area under applied voltage at room temperature (Fig. 5). In this case, an electrochemically non-active CS-AFM Pt tip with a size of approximately 50 nm (contact area) was used as the top electrode. By applying a negative voltage (0 to −2 V) to the initial 'OFF' state of the Fe_2O_3 NC film, randomly formed conducting paths (bright regions) were observed; these paths result in the high-current state through the 'SET' process (i.e., region (1) → (2) in Fig. 4a). However, the conducting paths within the Fe_2O_3 NC film were degraded because of the heating effect (i.e., 'RESET' process) [42], which lead to the low-current state (i.e., 'OFF' state, region (4) in Fig. 4a).

Although the switching mechanism in resistive switching memory devices is still controversial, a possible mechanism for the resistive switching behavior in our system can be proposed on the basis of the memristive model [14,15]. The positively charged carriers (i.e., Fe ions) in the Fe_2O_3 lattices are repelled or attracted from

the top electrode according to the electric field and can drift as a result of tunneling through a thin residual region (i.e., an undoped charge carrier region within Fe_2O_3). Therefore, a negative voltage applied to the top electrode attracts positively charged carriers in the Fe_2O_3 lattices. These charges drift in the electric field through the most favorable diffusion paths to form channels with high electrical conductivity. After more conductance channels penetrate the electronic barrier, the device is switched ON, thereby producing a symmetric *I–V* curve that is the result of tunneling through a thin insulating barrier. However, when a voltage with a reverse polarity is applied to the top electrode, the positively charged carriers in the conducting channel are repelled from the top interface, and the original electronic barrier is recovered. Recently, Kim et al. [43] suggested that both the time-dependent capacitance and the time-dependent resistance in the memristive model arose from Fe^{2+} and Fe^{3+} having different mobilities in the nanoparticle lattices. When a voltage with a reverse polarity was applied to the top electrode, the charged carriers were repelled from the top interface (low-current state).

The following alternate switching mechanism was recently reported: solid electrolytes sandwiched between an Ag (or a Cu) anode and an inert cathode can cause bipolar switching behavior via an electrochemical redox reaction based on the high mobility of Ag ions [16]. Furthermore, metal ion diffusion from the top electrode can form localized metal atom chains that bridge the electrode materials under an electric field. However, our device exhibited bipolar switching behavior with an electrochemically inert tungsten top electrode, as mentioned earlier. These results imply that the redox reaction based on the high mobility of Ag ions (from the Ag top electrode) is not directly related to the resistive switching behavior of Fe_2O_3 NC films.

4. Conclusion

We demonstrated for the first time that superparamagnetic Fe_2O_3 nanoparticle films prepared from calcinated PAH/ferritin multilayers have resistive switching memory properties under externally applied voltage. The resulting film devices exhibited low operating voltages (i.e., $V_{RESET} \sim +1.6 \pm 0.2$ V and $V_{SET} \sim -1.2 \pm 0.2$ V) with an ON/OFF ratio of approximately 10^3, an excellent cycling endurance of up to 10^5 s and a short switching speed of approximately 100 ns. This approach is important because it is based on an LbL assembly method using solution-processible proteins instead of synthesized inorganic or organic materials, which enables production of large-area inorganic oxide-based devices with excellent device performance and memory modulation.

Acknowledgements

This work was supported by the National Research Foundation (NRF) grant funded by the Ministry of Science, ICT, & Future Planning (MSIP) (2015R1A2A1A01004354).

Appendix A. Supplementary data

Supplementary data associated with this article can be found, in the online version, at http://dx.doi.org/10.1016/j.apsusc.2016.01.225.

References

[1] F.C. Meldrum, V.J. Wade, D.L. Nimmo, B.R. Heywood, S. Mann, Synthesis of inorganic nanophase materials in supramolecular protein cages, Nature 349 (1991) 684–687.
[2] T. Ueno, M. Suzuki, T. Goto, T. Matsumoto, K. Nagayama, Y. Watanabe, Size-selective loefin hydrogenation, Angew. Chem. Int. Ed. 43 (2004) 2527–2530.
[3] J.M. Dominguez-Vera, N. Gálvez, P. Sánchez, A.J. Mota, S. Trasobares, J.C. Hernández, J.J. Calvino, Size-controlled water-soluble Ag nanoparticles, Eur. J. Inorg. Chem. 30 (2007) 4823–4826.
[4] T. Douglas, V.T. Stark, Nanophase cobalt oxyhydroxide mineral synthesized within the protein cage of ferritin, Inorg. Chem. 39 (2000) 1828–1830.
[5] M. Tominaga, A. Ohira, A. Kubo, I. Taniguchi, M. Kunitake, Growth of carbon nanotubes as a gold (1 1 1) surface using two-dimensional iron oxide nano-particle catalysts derived from storage protein, Chem. Commun. (2004) 1518–1519.
[6] J. Polanams, A.D. Ray, R.K. Watt, Nanophase iron phosphate, iron arsenate, iron vanadate and iron molybdate minerals synthesized within the protein cage of ferritin, Inorg. Chem. 44 (2005) 3203–3209.
[7] E. Falvo, E. Tremante, R. Fraioli, C. Leonetti, C. Zamparelli, A. Boffi, V. Morea, P. Ceci, P. Ciacomini, Antibody–drug conjugates: targeting melanoma with cisplatin encapsulated in protein-cage nanoparticles based on human ferritin, Nanoscale 5 (2013) 12278–12285.
[8] D.P. Cormode, P.A. Jarzyna, W.J.M. Mulder, Z.A. Fayad, Modified natural nanoparticles as contrast agent for medical imaging, Adv. Drug Deliver Rev. 62 (2010) 329–338.
[9] I. Yamashita, K. Iwahori, S. Kumagai, Ferritin in the field of nanodevices, Biochim. Biophys. Acta 1800 (2010) 846–857.
[10] M.K. Shin, S.I. Kim, S.J. Kim, S.Y. Park, Y.H. Hyun, Y. Lee, K.E. Lee, S.-S. Han, D.-P. Jang, Y.-B. Kim, J.-H. Cho, I. So, G.M. Spinks, Controlled magnetic nanofiber hydrogels by clustering ferritin, Langmuir 24 (2008) 12107–12111.
[11] M. Kwon, H. Choi, M. Chang, M. Jo, S.-J. Jung, H. Hwang, Droplet evaporation-induced ferritin self-assembled monolayer as a template for nanocrystal flash memory, Appl. Phys. Lett. 90 (2007) 193512.
[12] A. Miura, R. Tanaka, Y. Uraoka, N. Natsukawa, I. Yamashita, T. Fuyuki, The characterization of a single discrete bionanodot for memory device applications, Nanotechnology 20 (2009) 125702.
[13] K. Nagashima, T. Yanagida, K. Oka, M. Taniguchi, T. Kawai, J.-S. Kim, B.H. Park, Resistive switching multistate nonvolatile memory effects in a single cobalt oxide nanowire, Nano Lett. 20 (2010) 1350–1363.
[14] J.J. Yang, M.D. Pickett, X. Li, D.A.A. Ohlberg, D.R. Stewart, R.S. Williams, Memristive switching mechanism for metal/oxide/metal nanodevices, Nat. Nanotechnol. 3 (2008) 429–433.
[15] D.B. Strukov, G.S. Snider, D.R. Stewart, R.S. Williams, The missing memristor found, Nature 453 (2008) 80–83.
[16] R. Waser, M. Aono, Nanoionics-based resistive switching memories, Nat. Mater. 6 (2007) 833–840.
[17] X. Zhu, W. Su, Y. Liu, B. Hu, L. Pan, W. Lu, J. Zhang, R.-W. Li, Observation of conductance quantization in oxide-based resistive switching memory, Adv. Mater. 24 (2012) 3941–3946.
[18] Y. Du, H. Pan, S. Wang, T. Wu, Y.P. Peng, J. Pan, A.T.S. Wee, Symmetrical negative differential resistance behavior of a resistive switching device, ACS Nano 6 (2012) 2517–2523.
[19] X. Chen, H.J. Feng, D. Bae, Drastic reduction of RRAM reset current via plasma oxidation of TaO_x film, Appl. Surf. Sci. 324 (2015) 275–279.
[20] B.J. Choi, D.S. Jeong, S.K. Kim, C. Rohde, S. Choi, J.H. Oh, H.J. Kim, C.S. Hwang, K. Szot, R. Waser, B. Reichenberg, S. Tiedke, Resistive switching mechanism of TiO_2 thin films grown by atomic-layer deposition, J. Appl. Phys. 98 (2005) 033715.
[21] L. Zou, W. Wu, W. Xie, R. Chen, N. Qin, B. Li, D. Bao, Excellent resistive switching property and physical mechanism of amorphous TiO_2 thin film fabricated by a low-temperature photochemical solution deposition method, Appl. Surf. Sci. 311 (2014) 697–702.
[22] W. Guan, D.S. Long, R. Jia, M. Liu, Nonvolatile resistive switching memory utilizing gold nanocrystals embedded in zirconium oxide, Appl. Phys. Lett. 91 (2007) 062111.
[23] Y. Yang, X. Zhang, M. Gao, F. Zeng, W. Zhou, S. Xie, F. Pan, Nonvolatile resistive switching in single crystalline ZnO nanowires, Nanoscale 3 (2011) 1917–1921.
[24] D. Ielmini, F. Nardi, C. Cagli, Physical models of size-dependent nanofilament formation and rupture in NiO resistive switching memories, Nanotechnology 22 (2011) 254022.
[25] M.-J. Lee, S. Han, S.H. Jeon, B.H. Park, B.S. Kang, S.-E. Ahn, K.H. Kim, C.B. Lee, C.J. Kim, I.-K. Yoo, D.H. Seo, X.-S. Li, J.-B. Park, J.-H. Lee, Y. Park, Electrical manipulation of nanofilaments in transition-metal oxides for resistance-based memory, Nano Lett. 9 (2009) 1476–1481.
[26] F. Verbakel, S.C.J. Meskers, R.A.J. Janssen, Surface modification of zinc oxide nanoparticles influences the electronic memory effects in ZnO-polystyrene diodes, J. Phys. Chem. C 111 (2007) 10150–10153.
[27] B.C. Das, S.K. Batabyal, A.J. Pal, A bit per particle: electrostatic assembly of CdSe quantum dots as memory elements, Adv. Mater. 19 (2007) 4172–4176.
[28] G. Decher, Fuzzy nanoassemblies: toward layered polymeric multicomposites, Science 227 (1997) 1232–1237.
[29] F. Caruso, R.A. Caruso, H. Möhwald, Nanoengineering of inorganic and hybrid sphere by colloidal templating, Science 282 (1998) 1111–1114.
[30] J. Cho, K. Char, J.-D. Hong, K.-B. Lee, Fabrication of highly ordered multilayer films using spin self-assembly method, Adv. Mater. 13 (2001) 1076–1078.
[31] J. Cho, F. Caruso, Investigation of the interactions between ligand-stabilized gold nanoparticles and polyelectrolyte multilayer films, Chem. Mater. 17 (2005) 4547–4553.
[32] J.-W. Kim, S.H. Choi, P.T. Lillehei, S.-H. Chu, G.C. King, G.D. Watt, Cobalt oxide hollow nanoparticles derived by bio-templating, Chem. Commun. (2005) 4101–4103.

[33] G. Wang, Y. Ling, D.A. Wheeler, K.E.N. George, K. Horsley, C. Heske, J.Z. Zhang, Y. Li, Facile synthesis of highly photoactive α-Fe_2O_3-based films for water oxidation, Nano Lett. 11 (2011) 3503–3509.
[34] Y. Gao, S.A. Chambers, Heteroepitaxial growth of α-Fe_2O_3, γ-Fe_2O_3 and Fe_3O_4 thin films by oxygen-plasma-assisted molecular beam epitaxy, J. Cryst. Growth 174 (1997) 446–454.
[35] A.A. Tahir, K.G.U. Wijayantha, S. Saremi-Yarahmadi, M. Nazhar, V. Mckee, Nanostructured α-Fe_2O_3 thin films for photoelectrochemical hydrogen generation, Chem. Mater. 21 (2009) 3763–3772.
[36] J. Lu, Z. Jiao, D. Chen, W. Li, Solvothermal synthesis and characterization of Fe_3O_4 and γ-Fe_2O_3 nanoplates, J. Phys. Chem. C 113 (2009) 4012–4017.
[37] X. Zhu, Y. Zhu, S. Murali, M.D. Stoller, R.S. Ruoff, Nanostructured reduced graphene oxide/Fe_2O_3 composite as a high-performance anode material for lithium ion batteries, ACS Nano 5 (2011) 3333–3338.
[38] T. Yamashita, P. Hayes, Analysis of XPS spectra of Fe^{2+} and Fe^{3+} ions in oxide materials, Appl. Phys. Sci. 254 (2008) 2441–2449.
[39] J. Baltrusaitis, D.M. Cwiertny, V.H. Grassian, Adsorption of sulfur dioxide on hematite and goethite particle surfaces, Phys. Chem. Chem. Phys. 9 (2007) 5542–5554.
[40] X. Qu, N. Kobayashi, T. Komatsu, Solid Nanotubes comprising α-Fe_2O_3 nanoparticles prepared from ferritin protein, ACS Nano 4 (2010) 1732–1738.
[41] Z. Sun, H. Yuan, X. Zhang, A highly efficient chemical sensor material for H_2S: α-Fe_2O_3 nanotubes fabricated using carbon nanotubes templates, Adv. Mater. 17 (2005) 2993–2997.
[42] D.-H. Kwon, K.M. Kim, J.H. Jang, J.M. Jeon, M.H. Lee, G.H. Kim, X.-S. Li, G.-S. Park, B. Lee, S. Han, M. Kim, C.S. Hwang, Atomic structure of conducting nanofilaments in TiO_2 resistive switching memory, Nat. Nanotechnol. 5 (2010) 148–153.
[43] T.H. Kim, E.Y. Jang, N.J. Lee, D.J. Choi, K.-J. Lee, J.-T. Jang, J.-S. Choi, S.H. Moon, J. Cheon, Nanoparticle assemblies as memristors, Nano Lett. 9 (2009) 2226–2233.